

15. Candelas, P., Horowitz, G. T., Strominger, A. & Witten, E. *Nucl. Phys.* **B258**, 46–74 (1985).
16. Calabi, E. in *Algebraic Geometry and Topology: a Symposium in Honor of S. Lefschetz* 78–89 (Princeton University Press, 1957).
17. Yau, S. T. *Proc. natn. Acad. Sci. U.S.A.* **74**, 1798–1799 (1974).
18. Witten, E. preprint, Princeton Univ. (1985).
19. Witten, E. *Nucl. Phys.* **B258**, 75–100 (1985).
20. Dine, M., Kaplunovsky, V., Mangano, M., Nappi, C. & Seiberg, N. *Nucl. Phys.* **B259**, 549–571 (1985).
21. Breit, J. D., Ovrut, B. A. & Segrè, G. *Phys. Lett.* **1** **158B**, 33–39 (1985).
22. Hosotani, Y. *Phys. Lett.* **126B**, 309–313 (1983).
23. Strominger, A. & Witten, E. *Commun. Math. Phys.* **101**, 341 (1985).
24. Ellis, J., Lahanas, A. B., Nanopoulos, D. V. & Tamvakis, K. *Phys. Lett.* **134B**, 429–435 (1984).
25. Ellis, J., Kounnas, C. & Nanopoulos, D. V. *Nucl. Phys.* **B241**, 406–428; **B247**, 373–395 (1984).
26. Derendinger, J.-P., Ibañez, L. & Nilles, H.-P. *Phys. Lett.* **155B**, 65 (1985).
27. Dine, M., Rohm, R., Seiberg, N. & Witten, E. *Phys. Lett.* **156B**, 55–60 (1985).
28. Cohen, E., Ellis, J., Enqvist, K. & Nanopoulos, D. V. *Phys. Lett.* **165B**, 76–82 (1985).
29. Barger, V., Deshpande, N. G. & Whisnant, K. *Phys. Rev. Lett.* **56**, 30–33 (1986).
30. Ellis, J., Enqvist, K., Nanopoulos, D. V. & Zwirner, Nucl. Phys. **B276**, 14–70 (1986); *Mod. Phys. Lett.* **A1**, 57–69 (1986).
31. Durkin, L. S. & Langacker, P. *Phys. Lett.* **166B**, 436–442 (1986).
32. Ellis, J., Enqvist, K., Nanopoulos, D. V. & Sarkar, S. *Phys. Lett.* **167B**, 457–463 (1986).
33. Steigman, G. A., Olive, K. A., Schramm, D. N. & Turner, M. S. *Phys. Lett.* **176B**, 33–38 (1986).

ARTICLES

Non-explosive silicic volcanism

J. C. Eichelberger, C. R. Carrigan, H. R. Westrich & R. H. Price

Sandia National Laboratories, Albuquerque, New Mexico 87185, USA

Silicic magma can erupt quietly, as vapour-poor lava, despite petrological evidence that it once contained ample dissolved water to drive violent venting of tephra. Non-explosive eruption of lava appears to result from rapid, sub-surface gas release from magma ascending as a permeable foam. The degassed foam then collapses during extrusion. Conditions of shallow ascent, rather than pre-eruption volatile concentrations, control eruptive behaviour.

SILICIC volcanic eruption sequences commonly begin with vigorous ejection of fragmental magmatic material consisting of pumice and ash, and conclude with quiet effusion of lava domes or flows. The explosive case is well described by considering exsolution of volatiles in magmatic melt during decompression, expansion of the magma as a foam, and subsequent fragmentation and further expansion of the magma as a dusty gas^{1,2}. No such theoretical treatment has been offered for the non-explosive case. The absence of fragmentation during extrusion clearly reflects a lower vapour content, but this may arise in two ways. If the magma behaves as a chemically closed system, then the extrusion of domes results from ascent of initially volatile-poor magma, and the transition from explosive to non-explosive behaviour reflects pre-eruption volatile gradients in the parent body³. This is a widely held view of the relationship between eruptive behaviour and pre-eruption magma composition. Alternatively, if the magma behaves as an open system during ascent, then the transition to non-explosive behaviour reflects a change in the conditions of ascent. Here we present a gas-dynamical model for dome-forming eruptions, involving open-system behaviour of magma on an eruptive timescale. Such a model necessarily proceeds from an accurate physical and chemical description of an appropriate igneous system. Research drilling into the 600-yr-old Obsidian Dome⁴, the largest dome of the Inyo Domes chain in eastern California, has recently provided information that could not be obtained from examining the surfaces of young domes and the intrusive roots of old ones. Although we base our discussion in part on results from this system, we believe that the model has general applicability.

Obsidian Dome

The physical characteristics of Obsidian Dome and the upper 600 m of its intrusive feeder are interpreted from surface observations and three continuously cored holes (Fig. 1). The first hole penetrated the distal portion of the dome, the second passed through the proximal section of the dome and the underlying intrusion that forms the dome's conduit, and the third intersected an unvented portion of the same intrusion, ~1 km to the south.

Obsidian Dome is pancake-shaped, 0.1 km³ in volume, 2 km in diameter, and 30–50 m thick at its margins. Near the vent, the thickness increases rapidly to 100 m. At a depth of 400–500 m, the conduit of the dome is 33 m wide. The conduit lies

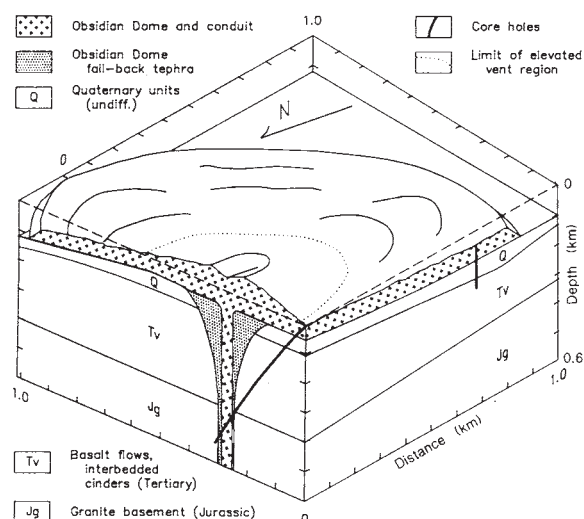


Fig. 1 Block diagram showing locations of the distal and proximal drill holes at Obsidian Dome and major intersected subsurface features. The origin of the plot is the wellhead of the proximal hole, which intersects the conduit of the dome; the two vertical planes contain the holes and form a 99° angle. A third hole, not shown, lies approximately on the right rear face of the block, and intersects an unvented portion of the feeder dike at 610–640 m depth.

within a broader vent structure, exceeding 50 m in width at the depth of observation, which contains fall-back tephra, slumped blocks of wall rock, and small co-magmatic intrusions. These materials are presumed to occupy the lower portion of a vent funnel which was excavated during the immediately preceding explosive phase of activity. One kilometre to the south, the intrusion is 7 m wide at a depth of 600 m, where it is in direct contact with Sierra Nevada granitic basement. The intrusion is evidently a long, thin dike which widens beneath the dome.

There are no apparent petrological differences between the explosively erupted tephra and non-explosively erupted dome,

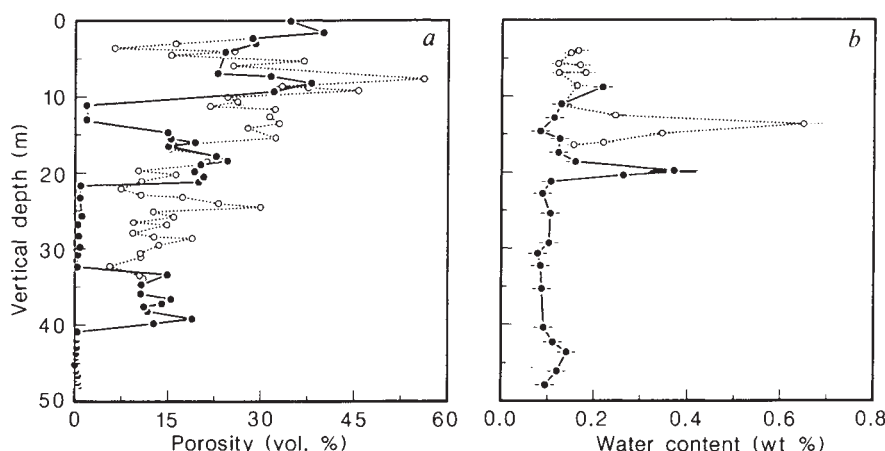


Fig. 2 Porosity (a) and water content (b) profiles through the distal (●) and proximal (○) portions of Obsidian Dome. a, Porosities were calculated from bulk and grain density measurements; replicate determinations gave errors (2 s.d.) of ± 0.3 vol. %. Porosity attributed to second boiling following emplacement (consisting of large voids associated with spheroidal regions of devitrification-lithophysae) is not included in the profiles. b, Water contents were determined for glassy samples by Karl Fischer titration. Error bars show 2 s.d., where larger than symbols. Peaks in water content near the top of both sections appear to reflect the adsorption on bubble walls at sub-magmatic temperature of magmatic water vapour escaping from the flow interior, because these samples are from bubble-rich zones and release water at relatively low temperature.

although differences would be expected if volatile concentrations varied greatly in the parent magma reservoir. The rocks range in composition from rhyolite to rhyodacite. Phenocrysts are <10% by volume and include the hydrous phases hornblende and biotite. In the dome, glass-rich zones extend 10–20 m inward from the top and bottom surfaces to a more crystalline central portion. In contrast, samples from the intrusion are completely crystalline, except for one 10-cm-thick glassy contact zone.

Porosity data (Fig. 2a) provide evidence of the final distribution of vapour in the system. Like all silicic domes, the surface of Obsidian Dome is pumiceous. At the dome margin, an obsidian (bubble-free glass) layer is exposed ~10 m below the flow top. Observations from the distal core hole show that obsidian comprises a large portion of the distal interior. However, obsidian is absent near the vent, where all the lava is vesicular. Similarly, no bubble-free material occurs in the intrusion, where most porosity values lie between 10 and 20%.

Water is the predominant volatile component in the glasses, and therefore the most important chemical component in determining eruptive behaviour. Figure 2b shows that the low values previously observed at the surface of the dome⁵ continue into the interior. Of special interest is the water content of the obsidian, as this material could not have changed chemically since emplacement. The retained magmatic water content of obsidian in the dome is everywhere close to 0.1 wt %. In contrast, the variable water contents of pumiceous lava probably reflect adsorption during cooling. None of the glass within the intrusion is sufficiently unaltered to allow the determination of magmatic water values. However, fresh, intrusion-derived glass fragments in nearby fractures yielded water contents of 1.15 and 1.21 wt % at depths of 290 and 370 m, respectively.

Compositional path of ascending magma

The above observations can be used to determine whether the water content of the dome-forming magma changed during ascent. The pre-eruption water content is constrained by the phenocryst assemblage, the surface-emplacement water content can be directly determined from the obsidian, and inferences about water content at intervening depths can be drawn from characteristics of the intrusion. Experiments⁶ in a synthetic system similar to Obsidian Dome show the dependence of liquidus temperature and hornblende stability on water content at 2 and 8 kbar. Liquidus temperature declines steeply from >1,200 °C in the anhydrous system to 1,000 °C at 4 wt % water. Hornblende becomes stable at water contents of 3–4 wt %. Higher pressure does not appreciably affect the liquidus or the minimum water content at which hornblende is stable. The low phenocryst content indicates that the magma was near its liquidus at ~950 °C (as determined by Fe–Ti oxide thermometry;

ref. 7). The phenocryst assemblage thus requires ≥ 3 wt % water in melt before ascent.

Figure 3 shows what happens to magma with 3 wt % water as it approaches the surface. We can assume that the ascending magma is under a confining pressure close to lithostatic because of the fractured nature of the intruded environment. The condition for stability of vapour bubbles in the magma is that the vapour pressure in the bubbles equals the confining pressure on the magma. Bubble growth occurs in response to excess vapour pressure, but the required excess in hydrous magma is believed to be small¹. Bubble content increases with decreasing depth because confining pressure decreases, causing water to become less soluble in melt and the vapour to expand. For the system of interest, bubble growth begins at 500 bar, or ~2.5 km depth, and the bubble:melt ratio reaches 3:1 at ~400 m depth. This degree of inflation is important because significantly higher porosities are seldom observed in ejecta¹. The stretched and weakened bubble walls apparently fail at this point, and an explosive eruption follows. The dome magma did not reach fragmentation conditions, although its equilibrium bubble:melt ratio at 3 wt % water would have been 400:1 on reaching the surface or, alternatively, its excess pore pressure at observed porosities and 3 wt % water would have been 100–500 bar.

If we consider the final composition of the dome magma as represented by the obsidian, we find that the water content is consistent with an absence of bubbles in melt under the existing loads of 2–10 bar. However, it is apparent from the above discussion that the phase assemblage must be regarded as relict from a much more water-rich system. The liquidus temperature at 0.1 wt % would exceed 1,200 °C, in conflict with Fe–Ti oxide compositions, and hornblende would not be stable at any temperature. Instead, the observed water content suggests open-system equilibration with surface conditions, because it corresponds closely with the expected solubility of water in melt at atmospheric pressure⁸. Furthermore, the hydrogen isotopic composition of the water lies at the end-point of a trend defined by more water-rich explosive ejecta, which is best explained by open-system Rayleigh fractionation of hydrogen isotopes between melt and vapour during the release of water⁵.

The loss of water during ascent is also indicated by two features of the intrusion. First, the boundary glass zones are more than two orders of magnitude thicker in the dome than in the intrusion, and are entirely absent from the conduit. This cannot be explained by thermal history because the relative sizes indicate that the intrusion cooled as fast as, or faster than, the dome⁹. As water facilitates crystallization in rhyolitic systems¹⁰, greater retention of water at depth would explain the contrast in crystallinity between the dome and its feeder. Second, vesicles that appear to be primary occur throughout the intrusion. Their existence as water vapour bubbles would require at least 1 wt %

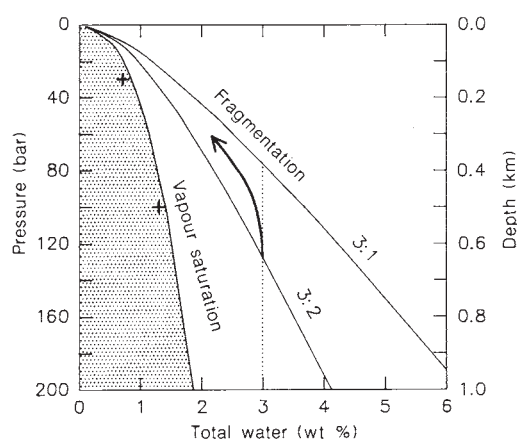


Fig. 3 Total magmatic water content for crystal-poor rhyolite magma as a function of pressure and depth in the uppermost 1 km. Ideal gas behaviour of water and solubility relations as described by Burnham¹⁹ are assumed. The depth dependence involves the additional assumptions of pressure equilibrium between lithostatic load and vapour pressure, and an average bulk density of overburden of 2 g cm^{-3} . The vapour-undersaturated region is shaded. Two values (crosses) from the solubility approximation (equation (3)) used by Sparks¹ are shown; this approximation is used in subsequent calculations. Two curves describe the system at bubble:melt ratios of 3:2 (60% porosity) and 3:1 (75% porosity). The latter curve is believed to mark the onset of fragmentation. Magma that behaves as a chemically closed system during ascent will follow a vertical path (dotted line) and fragment to form tephra. The inferred behaviour of dome magma is indicated by the arrow.

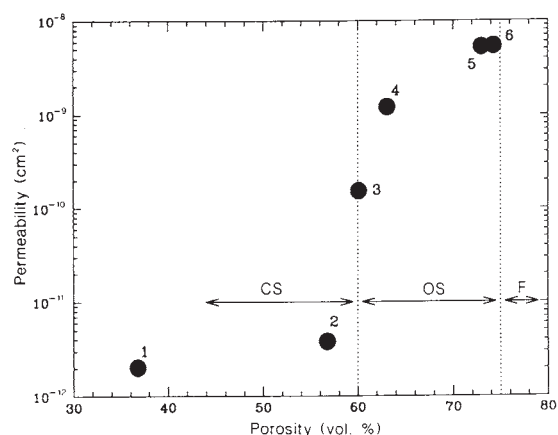


Fig. 4 Gas permeability and porosity for Inyo rhyolite and related samples. Gas permeabilities were determined with nitrogen at room temperature, using confining pressures of 3–50 bar and input pressures of 1.2–50 bar. Less permeable samples required higher pressures. The confining pressure was varied to check for leakage between the sample and the jacket. The range of permeabilities over a variety of flow conditions is nowhere greater than the symbol size. Samples are from: 1, proximal hole, 5.3 m depth; 2, proximal hole, 14.3 m depth; 3, proximal hole, 13.9 m depth; 4, 5, Panum Dome, surface; 6, Large pumice block, explosive phase of Inyo eruption (Glass Creek vent), collected 1 km south-west of Obsidian Dome. Porosity regimes: CS, closed system; OS, open system; F fragmentation.

water in the coexisting melt (Fig. 3), consistent with the 1.2 wt % water observed in the glass fragments. If formed secondarily during crystallization (second boiling), more water than is present in the obsidian would be required to produce the observed porosity.

These considerations require that the dome magma lost most of its water during ascent, and that the magma extruded as Obsidian Dome lost more water than the magma emplaced at 400–600 m depth.

Physical conditions of water release

Observations at Obsidian Dome also provide evidence of the process by which water release occurs, and the time and distance scales over which the process operates. Degassing must occur on an eruptive timescale, otherwise the magma would fragment during ascent. The timescale of ascent and hence decompression is severely constrained by the small volume of the feeder relative to the dome. If the dome was extruded in a year or less¹¹, and the conduit is twice as long along the dike trend as its intersected width, then the dome magma underwent the final 100 bar of decompression in two days or less. Magma in the form represented by obsidian could not change chemically on this timescale, because mass transport would have to occur exclusively by the exceedingly slow process of diffusion in melt¹². However, the increasing porosity of the dome as the vent is approached (Fig. 2a) suggests that the magma was extruded as a foam that collapsed as it flowed outwards. Indeed, the ascent of magma as a foam is required by the inferred initial water content. If the bubbles of the foam were connected, then volatiles could escape the system by a two-step process. The first step involves diffusion of volatiles through melt into bubbles, and the second the flow of gas from bubble to bubble and out of the system. The first step occurs over micrometres and requires seconds¹. The second occurs over metres, and calculation of the timescale requires knowledge of the permeability of the magmatic foam.

Once out of the magma, gas could easily escape into the 'sand-pile' environment of finely fragmented material provided by the vent funnel.

No direct measurements of permeability of vesicular, non-fragmental magmatic material have previously been made, although Witham and Sparks¹³ inferred high permeability from the behaviour of pumice in water. Figure 4 shows the gas permeability of Obsidian Dome and related rhyolite over the porosity range 37–74%. The permeability increases by three orders of magnitude during the expansion of bubbles from 55 to 75 vol. % of the system. Hence, the bubbles become well interconnected during ascent before the fragmentation regime is reached—at depths of $\geq 500 \text{ m}$ for magma with the inferred water content of $\geq 3 \text{ wt } \%$ (Fig. 3).

Porous-flow model

The escape of gas from a foam can be modelled using a combined analytical and numerical approach. The ascending magma is treated as a dike, with outward horizontal gas flow symmetrical about its centre-line, where the flux is zero. A constant, zero gas pressure is applied at the margins, to simulate the large discontinuity in permeability which exists between the porous magma, which provides some resistance to gas flow, and the more permeable fragmental material of the vent funnel, into which the magma has intruded. The gas flow is described by Darcy's law¹⁴, which relates the pore velocity u to the pressure gradient dP/dx , through the porosity ϕ , the permeability K , and the gas viscosity μ :

$$\phi u = -\frac{K}{\mu} \frac{dP}{dx} \quad (1)$$

The amount of gas vapour in an elementary volume is given by a conservation equation:

$$\phi \frac{\partial \rho_v}{\partial t} = -\phi \frac{\partial}{\partial x} \rho_v u + \rho_m (1 - \phi) \frac{d\chi}{dP} \frac{\partial P}{\partial t} \quad (2)$$

where ρ_v and ρ_m are the vapour and melt densities, respectively,

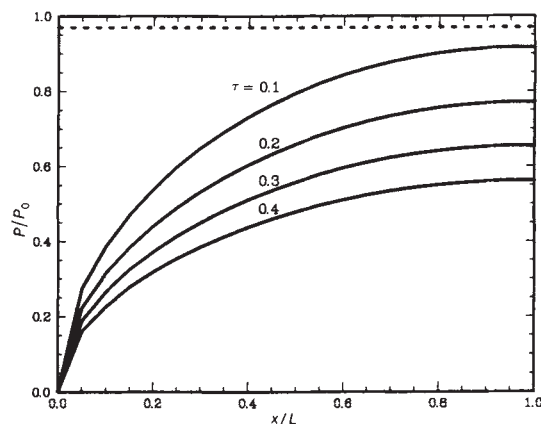


Fig. 5 Calculated vapour pressure profiles in magma across the half-width of a dike, at various times (τ) after the onset of degassing. Vapour pressure, position and time are expressed as dimensionless variables. Distance increases from the edge of the dike ($x/L=0$) to the centre-line ($x/L=1.0$). The scalings are: P_0 , the initial vapour pressure; L , the half-width of the dike; and $\mu L^2 \phi / k P_0$, the gas diffusion timescale. Note that time scales with the square of the dike half-width. For Obsidian Dome we use $P_0 = 100$ bar, $L = 1,650$ cm, $\mu = 4.3 \times 10^{-4}$ poise (water vapour at 900°C), $\phi = 0.67$, and $K = 0.2 \times 10^{-8}$ cm². Thus, to obtain the Obsidian Dome case, multiply (P/P_0) by 100 to obtain bars, (x/L) by 16.5 to obtain metres, and τ by 2,600 to obtain seconds. The four profiles are then at 375, 750, 1,125 and 1,500 s. At 1,500 s, the load on the magma ascending at 1 cm s^{-1} has decreased by only 3 bar (indicated by the dashed line), but the vapour pressure has decreased by >40 bar.

t is time, and χ is the weight fraction of water in the melt. Equation (2) relates the time rate of change of the local vapour density to the divergence of the mass flow rate, and a pressure-dependent vapour source term which takes into account the exsolution of volatiles from the melt. Sparks' approximation¹ for the relationship between equilibrium melt water content and vapour pressure,

$$\chi = aP^{1/2} \quad (3)$$

where $a = 0.0013 \text{ bar}^{-1/2}$, permits the evaluation of the vapour source term. Finally, the ideal gas law provides a satisfactory description of water vapour expansion². Combining equations (1)–(3) and the ideal gas law, we obtain a dimensionless equation for vapour pressure as a function of time:

$$\frac{\partial P}{\partial t} = \frac{P^{1/2}}{P^{1/2} - C} \frac{\partial}{\partial x} P \frac{\partial P}{\partial x} \quad (4)$$

where $C = [\rho_m(1-\phi)RTa]/2\phi P_0^{1/2}$, R is the gas constant, T is temperature, and P_0 is the vapour pressure at $t=0$. This equation may be solved numerically over the half-width of the dike for the stated boundary conditions (Fig. 5).

To apply the solution to a given eruptive event, the relevant physical parameters are needed to evaluate the scalings for pressure, time and horizontal coordinate. If we assume that degassing begins as magma enters the base of the vent funnel and that this depth at Obsidian Dome is 500 m, then the bubble:melt ratio of the magma will be $\geq 2:1$ (Fig. 3) and the permeability will be $\geq 0.2 \times 10^{-8} \text{ cm}^2$ (Fig. 4). These values lie between the opening of the system to gas flow and fragmentation. The use of this value of porosity implies that significant bubble collapse occurred following degassing, particularly in the magma comprising the conduit and distal portion of the dome, but this is consistent with the central depression in the vent region and rapid decrease in dome thickness away from the vent region (Fig. 1). The half-width used, 16.5 m, is derived from the drilling results. Other values of physical properties used in the

scalings are typical for rhyolitic magma (for example refs 1 and 12).

We can now ask whether degassing is sufficiently rapid to prevent further bubble growth, which would lead to fragmentation. Bubble growth will not occur if the vapour pressure declines as fast or faster than the lithostatic load on the ascending magma. A reasonable upper bound for the ascent rate is 1 cm s^{-1} (dome formation in 2 months), corresponding to a decompression rate of $\sim 0.002 \text{ bar s}^{-1}$. The calculation shows that pore pressure declines at 0.03 bar s^{-1} , an order of magnitude faster (Fig. 5). Although we have simplified the problem by keeping porosity and permeability constant, the calculation demonstrates that if the magma ascends through an environment in which gas can escape freely, it cannot reach the degree of inflation observed in the explosive ejecta. Instead, the magma inflates until the contributions to bubble volume from vapour exsolution and expansion are balanced by increasingly rapid vapour loss, and arrives at the surface fully degassed (Fig. 3). Vertical gas flow may predominate late in the ascent.

The uniform 0.1 wt % water content of obsidian in the dome shows that the extruding foam was rather stiff. The vapour pressure throughout the dome bled off to near-atmospheric pressure before bubble collapse began. This left the system water-undersaturated when pressure equilibrium was re-established, so that the small amount of vapour remaining, 0.02 wt % at 50% porosity, was readily resorbed to produce bubble-free obsidian. Had bubble collapse restored the equilibrium between lithostatic load and pore pressure before degassing was complete, then the water content under the 10-bar load near the base of the dome would be measurably higher ($\sim 0.5 \text{ wt %}$; Fig. 3). The pumiceous carapace did not undergo collapse because of rapid cooling and a load pressure of <2 bar. The process is analogous to welding in ash-flow tuffs, which can produce obsidians without bubbles or even relict bubble textures¹⁵, and with water contents identical to dome obsidians⁸. The heat required for welding¹⁶ is better conserved in a dome than in a pyroclastic deposit.

Discussion

Our model indicates that conditions during final ascent, when silicic magma is permeable to gas flow ($\leq 1 \text{ km}$ depth for the commonly postulated water contents of 3–5 wt %^{17,18}) will determine whether an explosive eruption occurs. The development of a tephra-filled vent funnel during initial explosive events provides the high-permeability environment necessary for subsequent lava extrusion. Thus, a decrease in the explosivity of events does not demonstrate volatile zonation in the deep parent reservoir. The high permeability of vent funnels may be short-lived, however, because the fall-back tephra will itself tend to weld. Thus, activity that does not quickly follow funnel formation may revert to vent-clearing explosions. The fact that all large-volume silicic eruptions are explosive may reflect the exponential increase in degassing time with width of the ascending body (Fig. 5). The largest known rhyolitic lava flows have volumes of $<10^2 \text{ km}^3$ (ref. 20), whereas the volumes of individual explosive rhyolitic eruptions range to $>10^3 \text{ km}^3$ (ref. 21). It appears likely that magma in such large eruptions, rising through conduits of perhaps $\geq 100 \text{ m}$ in width, cannot degas sufficiently during ascent to prevent explosive fragmentation.

This view of silicic volcanism solves the paradox posed by the contrasting vapour content but petrological similarity of co-magmatic tephra and dome eruptions^{22–24}. It should motivate a re-examination of the shallow intrusive environment in relation to eruptive behaviour.

We are grateful for help and suggestions from David McTigue, Melvin Baer, Mark Stavig, Shigeo Aramaki, Peter Lipman and Stephen Sparks. This work was supported at Sandia National Laboratories by the US Department of Energy under contract DE-AC04-76DP00789.

Received 28 March; accepted 6 August 1986.

1. Sparks, R. S. J. *J. Volc. geotherm. Res.* **3**, 1-38 (1978).
2. Wilson, L. *J. Volc. geotherm. Res.* **8**, 297-313 (1980).
3. Fink, J. H. *Geol. Soc. Am. Bull.* **94**, 362-380 (1983).
4. Eichelberger, J. C., Lysne, P. C., Miller, C. D. & Younker, L. W. *Eos* **66**, 186-187 (1985).
5. Taylor, B. E., Eichelberger, J. C. & Westrich, H. R. *Nature* **306**, 541-545 (1983).
6. Nancy, M. T. *Am. J. Sci.* **283**, 993-1033 (1983).
7. Vogel, T. A., Schuratz, B. C. & Younker, L. W. *Eos* **66**, 384 (1985).
8. Fijlheraer, I. C. & Westrich, H. R. *U.S. Geol. Surv. Open File Rep. No. 84-939* 147-150 (1984).
9. Kasameyer, P. W., Younker, L. W., Eichelberger, J. C., Lysne, P. C. & Vogel, T. A. *Eos* **66**, 385 (1985).
10. Tuttle, O. F. & Bowen, N. L. *Mem. geol. Soc. Am.* No. 74 (1958).
11. Macdonald, G. A. *Volcanoes* (Prentice-Hall, Englewood Cliffs, 1972).
12. Shaw, H. R. *Publs. Carnegie Instn* **634**, 139-170 (1974).
13. Witham, A. G. & Sparks, R. S. *Bull. volc.* (in the press).
14. Bird, R. B., Stewart, W. E. & Lightfoot, E. N. *Transport Phenomena* (Wiley, New York, 1960).
15. Ross, C. S. & Smith, R. L. *Prof. Pap. U.S. geol. Surv.* **366**, 1-77 (1961).
16. Riehle, J. R. *Geol. Soc. Am. Bull.* **84**, 2193-2216 (1973).
17. Whitney, J. A. *J. geol.* **83**, 1-31 (1975).
18. Ritchey, J. L. *J. Volc. geotherm. Res.* **7**, 373-386 (1980).
19. Burnham, C. W. in *Geochemistry of Hydrothermal Ore Deposits* (ed. Barnes, H. L.) 71-136 (Wiley, New York, 1979).
20. Christiansen, R. L. *U.S. Geol. Surv. Open File Rep. No. 84-939*, 743-783 (1984).
21. Lipman, P. W. *J. geophys. Res.* **89**, 8801-8841 (1984).
22. Lipman, P. W. *J. Geol.* **79**, 438-456 (1971).
23. Bacon, C. R. *J. Volc. Geotherm. Res.* **18**, 57-115 (1983).
24. Ewart, A., Hildreth, W. & Carmichael, I. S. E. *Contr. Miner. Petrol.* **51**, 1-27 (1975).

LETTERS TO NATURE

Variable radio source GT0116+622 is a possible counterpart to Cas γ -1

P. C. Gregory*, N. Duric*, A. Reid*, J. Picha*,
T. Stevenson* & A. R. Taylor†

* Department of Physics, University of British Columbia, Vancouver,
British Columbia, Canada V6T 1W5

† Kapteyn Astronomical Institute, University of Groningen,
9700 AV Groningen, The Netherlands

Identification of celestial γ -ray sources has proved to be very difficult because of the large positional uncertainties (typically several degrees) and the transient nature of many of these objects. Highly variable radio emission is a striking characteristic of the most secure source of very high-energy radiation, Cygnus X-3 (ref. 1). Here we report the discovery of another highly variable radio source which coincides in position with the transient TeV γ -ray source Cas γ -1. We have obtained an accurate radio position with the Very Large Array (VLA) telescope but no optical counterpart was found on the Mount Palomar Sky Survey prints. We have also obtained upper limits on radio emission from the binary X-ray pulsar, 4U0115+634, another proposed identification for Cas γ -1.

The variable radio source GT0116+622 was discovered during the University of British Columbia (UBC) galactic radio patrol project²⁻⁴ carried out between 1977 and 1984 with the National Radio Astronomical Observatory (NRAO) 91-m telescope at a wavelength of 6 cm. The aim of this project was to survey repeatedly a strip along the galactic plane ($l = 40^\circ$ to

220° , $b \leq \pm 2^\circ$) for transient radio sources. In the survey area of ~ 500 square degrees, 32 variables and 27 possible variables were detected. Cyg X-3 was the only previously known source in this sample. Short term variables make up 64% of the sample (timescale of a few days) and among these, GT0116+622 exhibits the fourth largest degree of variability following Cyg X-3, GTO351+543a and GT0236+610. The probability of a chance detection of a short-term variable radio source comparable to GT0116+622 in the $1^\circ \times 1^\circ$ γ -ray error box is ~ 0.008 .

Table 1 lists 53 daily flux density measurements of the source between 1977 and 1984. Over this period the flux density varied from ≤ 5 to 73 mJy. The extensive coverage of the observations in 1977 and 1984 shows significant variability on timescales as short as 1 day with some evidence for a characteristic timescale of 5 days.

Ten-minute photographic VLA observations in A configuration were obtained on 1 January 1985 at 6 and 20 cm. A single unresolved source was detected at both wavelengths within the positional uncertainty of the radio patrol results. The observations were self-calibrated and the resulting maps noise-limited at both wavelengths to a dynamic range of $\sim 200:1$. The measured flux densities are: 20-cm flux density = 57.0 ± 0.5 mJy; 6-cm flux density = 40.5 ± 0.5 mJy. The 6-cm VLA flux density corresponds to about the middle of the range observed in the patrol measurements. The spectral index between 20 and 6 cm of $\alpha = -0.3$ is typical of many compact synchrotron-emitting variable radio sources, both galactic and extragalactic.

Table 2 compares our VLA position for GT0116+622 with the best position for Cas γ -1 obtained by Stephanian *et al.*⁵. We also include the position of a nearby binary X-ray pulsar, 4U0115+634, suggested⁶ as a possible counterpart to Cas γ -1. The position for 4U0115+634 is taken from ref. 7.